Improved Desalination by Polymer Grafting

Mamta Yadav,[1] Clifford E. Woodward,[2] and Jan Forsman[1]
[1]Theoretical Chemistry, Chemical Centre, Lund University, P.O. Box 124, S-221 00 Lund, Sweden
[2]School of Chemistry University College, University of New South Wales, ADFA Canberra ACT 2600, Australia

(Received 20 April 2026; accepted 14 October 2026; published 16 November 2026)

Freshwater scarcity demands desalination technologies that are efficient, scalable, and sustainable. Capacitive deionization (CDI) is promising but remains limited by inefficient ion adsorption and poor charge utilization. Here, we show that suitably chosen polyampholytic block copolymer grafting to the internal pore surfaces of CDI electrodes can substantially enhance CDI performance, via a combination of dipolar response and steric effects. Using mean-field classical density functional theory and grand-canonical Monte Carlo simulations, we demonstrate that such polymer grafted electrodes enable strongly improved desalination performance, without altering the pore width and geometry. Even an electrode grafting by simple neutral polymers can generate an improvement, although a suitably designed diblock polymer sequence offers an additional performance gain. These results establish interfacial block copolymer grafting as a powerful route toward high-performance, membrane-free desalination.

DOI: 10.1103/zkrf-mcwf

Introduction—Access to safe drinking water is declining globally [1]. Growing populations, industrial expansion, and agricultural intensification place unprecedented pressure on freshwater resources [2,3]. Although nearly 70% of Earth is covered by water, most is saline and unsuitable for direct human use [4,5]. Established desalination technologies, including thermal distillation [6], reverse osmosis [7], and electrodialysis [8], enable large-scale freshwater production, but their high energy demand limits long-term sustainability [9,10].

Capacitive deionization (CDI) has emerged as an energy efficient and cost effective route toward scalable and sustainable freshwater production [11,12]. By exploiting electric double layer charging in porous electrodes, CDI enables reversible electrosorption and release of ions under an applied potential [13–16]. We will in this Letter measure "performance" by the number of ions that can be extracted for a given energy input (per unit area). This will be quantified below. Conventional CDI electrodes based on activated carbon are fundamentally limited by low charge efficiency. Considerable effort has therefore focused on improving electrode materials [17,18]. Nanostructured carbons such as graphene derivatives and carbon nanotubes provide enhanced conductivity and accessible surface area, while emerging materials including MXenes offer larger salt adsorption capacities [19–22]. Despite these advances, CDI remains constrained by nonselective ion desorption. Membrane CDI (MCDI) partially addresses this issue by introducing ion-exchange membranes that suppress co-ion leakage and enhance salt removal [23]. Similarly, flow-electrode CDI (FCDI) enables continuous desalination [24]. However, FCDI suffers from low charge efficiency and electrode degradation, while MCDI is limited by weak electrode-membrane adhesion and increased contact resistance. Even designs incorporating ion-exchange polymers yield only marginal improvements [25–27].

Block copolymer based porous carbon fibers improve CDI performance by optimizing ion accessible surface area and transport routes, but rely on bulk structural optimization of electrode materials [28,29]. In contrast, polymer grafting controls interfacial chemistry and ion-surface interactions without altering pore architecture. A recent study showed that grafting conductive polymers onto activated carbon and MnO_2 electrodes enhances desalination capacity and kinetics through pseudocapacitive ion storage [30]. These results establish interfacial polymer functionalization as a promising route toward membrane free CDI. In this Letter, we demonstrate that block copolymer grafted electrodes reshape ion adsorption and significantly enhance desalination performance. This is supported by desalination loops from classical density functional theory (cDFT) and grand-canonical Monte Carlo simulations. Surprisingly, even neutral polymer grafts can increase desalination efficiency, although a block charge architecture leads to an additional gain.

Model and theory—We investigate the negative electrode and propose a "reversed" treatment at the positive electrode. We model electrode pores as slits, with infinite parallel walls separated by H. The walls carry a uniform

Published by the American Physical Society under the terms of the Creative Commons Attribution 4.0 International license. Further distribution of this work must maintain attribution to the author(s) and the published article's title, journal citation, and DOI. Funded by Bibsam.

surface charge density σ_s, determined by electroneutrality for an input applied electrode potential. Although real activated-carbon electrodes possess complex porous networks, the slit-pore geometry serves as a minimal model to isolate the interfacial physics introduced by polymer grafting. Realistic pore morphologies may modify the quantitative desalination performance while leaving the underlying steric and dipolar enhancement mechanism qualitatively unchanged. Following earlier cDFT work [16], we denote the electrode volume by V_e and the "bucket," to be desalinated, volume by V_b. We define $\xi = V_e/(V_e + V_b)$. We work under Ψ control, where Ψ is the applied electrode (Donnan) potential. We compare two cases, where the electrodes are either bare (reference) or carry overall electroneutral grafted polymers. The grafted chains have a block charge structure, where the end monomer of the positive block (with one bonded neighboring monomer) is grafted to the electrode.

We might write $|++++----$ as a pictorial illustration of grafted 8-mers $(4+4)$, where "|" describes the planar electrode surface to which the "leftmost" positive monomer is grafted. We will also explore grafted polymers where all monomers are electroneutral. The fixed bond length (but rotationally flexible) between connected monomers is set to $b = 6$ Å. Moreover, all simple ions and monomers have a hard-sphere (HS) diameter of $d = 4$ Å. These values represent typical coarse-grained molecular length scales and are not intended to describe a specific system. In Appendix B, we also explore vanishing hard cores for all species. The densities of positive and negative monomers are denoted n_+ and n_-.

Consider a polymer of r monomers. Denoting monomer i by $\mathbf{r}_i$, we represent a polymer configuration by $\mathbf{R} = (\mathbf{r}_1, \ldots, \mathbf{r}_r)$. We introduce a multipoint density distribution $N(\mathbf{R})$, such that $N(\mathbf{R})d\mathbf{R}$ is the number of polymer molecules with configurations between $\mathbf{R}$ and $\mathbf{R} + d\mathbf{R}$. Chain monomers are connected by bonds described by the bonding potential $\Phi_b(\mathbf{R})$. Rotationally unrestricted bonds of fixed length b imply that $e^{-\beta\Phi_b(\mathbf{R})} \propto \prod \delta(|\mathbf{r}_{i+1} - \mathbf{r}_i| - b)$, where $\delta(x)$ is the Dirac delta function, and $\beta = 1/(k_B T)$ is the inverse thermal energy.

For planar charged surfaces separated by H, we assume cylindrical symmetry about the surface-normal z axis. This allows us to integrate over the x, y coordinates, leaving only z-dependent quantities. Combined with the fixed bond length, this simplifies our representation of polymer density distributions:

$$N(\mathbf{Z}) = \prod_{i=1}^{r-1} \int N(\mathbf{R}) dx_{i+1} dy_{i+1}. \tag{1}$$

We use repeated cylindrical integrations, noting that $\int \delta(|\mathbf{r}_{i+1} - \mathbf{r}_i|) dx_{i+1} dy_{i+1} = 2\pi\Theta(b - |z_{i+1} - z_i|)$, where $\Theta(x)$ is the Heaviside step function. Thus, as a monomer rotates along the x, y ring at fixed bond length and z, we assume that the statistical (Boltzmann) weight is unchanged. We employ the following grand potential per unit area ω, for grafted r–mer chains, composed of charged blocks [15,31,32]:

$$\begin{aligned}
&\beta\omega(T, \phi_g, \mu_c, \mu_a, \Psi; [N(\mathbf{Z}), n_c(z), n_a(z)]) \\
&= \int N(\mathbf{Z})(\ln[N(\mathbf{Z})] - 1) d\mathbf{Z} + \beta \int N(\mathbf{Z}) \Phi_b(\mathbf{Z}) d\mathbf{Z} + \int n_c(z)(\ln[n_c(z)] - 1) + n_a(z)(\ln[n_a(z)] - 1) dz \\
&\quad + \beta \int \mathcal{F}_{\mathrm{HS}}^{(ex)}(n_+, n_-, n_c, n_a) dz + \frac{\beta e}{2} \int \psi(z) q(z) dz - \beta \int (\mu_c n_c(z) + \mu_a n_a(z)) dz + \beta \int n_+^e(z) \phi_g dz,
\end{aligned} \tag{2}$$

where e is the elementary charge, z denotes the coordinate perpendicular to the surfaces, $\mathbf{Z} = z_1 \ldots z_r$, $N(\mathbf{Z})$ is the polymer density distribution, and $\psi(z)$ is the local mean-field potential at z, *including* the applied electrode potential Ψ. The grafting potential ϕ_g acts only on positive end monomers, with a density $n_+^e(z)$. This grafting potential constrains these positive end monomers to a region within one bond length (b) from the surface to which they are bonded, and has a strength adjusted to arrive at the target grafting density. We use a fixed grafting density, κ, such that $\kappa = \int n_+^e(z) dz = 0.02/\text{Å}^2$. This value is partly ambiguous, but chosen to ensure a dense brush. In Appendix C, we compare with a lower grafting density. The anion and cation densities are denoted n_a and n_c, and their chemical potentials are μ_a and μ_c (note that $\mu_a = \mu_c$ since they have the same size and absolute valency; i.e., we adopt the "restricted primitive model" (RPM). The net charge distribution at z is denoted $q(z)$, i.e. $q(z) = e[n_c(z) + n_+(z) - n_a(z) - n_-(z)] + \sigma_s[\delta(z) + \delta(H - z)]$. Excluded volume effects are managed by $\mathcal{F}_{\mathrm{HS}}^{(\mathrm{ex})}(n_+, n_-, n_c, n_a)$, where we have utilized the generalized Flory-Dimer approximations [33]. The centers of mass of monomers and simple ions are confined to the region $d/2 < z < H - d/2$. All calculations were performed at a temperature $T = 298$ K, representing the aqueous solvent implicitly, via the dielectric constant, $\epsilon_r = 78.3$. The equilibrium grand potential per unit area, $\omega_{\mathrm{eq}}(H)$, was obtained by numerical minimization with respect to $N(\mathbf{Z})$, $n_c(z)$, and

$n_a(z)$, subject to conditions of electroneutrality and fixed grafting density. We utilized Picard iterations and well established numerical methods for polymer-cDFT [31,34]. The desalination loop starts at $\Psi = 0$. With $\langle n_c \rangle$ and $\langle n_a \rangle$ representing the average (free) cation and anion concentrations within V_e, we have at $\Psi = 0$ under full grand canonical conditions:

$$n_{\text{tot}} = 2n_s(1-\xi) + \xi(\langle n_c \rangle + \langle n_a \rangle), \tag{3}$$

where n_s is the salt concentration in the bucket (initially at 0.6 M) and n_{tot} represents the overall density of simple ions, averaged across the bucket and electrode volumes. Thus, n_{tot} is determined at this initial state by the presence of grafted polymers (or not), surface separation (H), and ξ.

From this starting state, we turn on a (negative) Donnan potential and trace two paths: (i) a full grand canonical path where there is complete chemical equilibrium with a bulk at a fixed concentration of 600 mM. (ii) A desalination path, where we gradually drain the "bulk"; i.e., the chemical potential is allowed to vary, and the appropriate value is found by an iterative procedure:

$$n_s(\mu_c, \Psi) = \frac{1}{2(1-\xi)}(n_{\text{tot}} - \xi(\langle n_c(\mu_c^{\text{eff}}) \rangle + \langle n_a(\mu_a^{\text{eff}}) \rangle)) \tag{4}$$

where $\mu_c^{\text{eff}} = \mu_c - e\Psi$ and $\mu_a^{\text{eff}} = \mu_a + e\Psi$ with e denoting the elementary charge and $\mu_c = \mu_a$ representing the ion chemical potentials in the bulk. At each applied potential, the chemical potential is adjusted iteratively until the bucket concentration n_s from Eq. (4) is consistent with the corresponding bulk salt chemical potential. The desalination process ends when n_s reaches the target concentration, here chosen as 1.2×10^{-5} Å^{-3} (~20 mM). This represents a typical low-salinity condition for potable water. The full cycle is illustrated via a cartoon in Appendix D.

An example of a desalination loop—Let us start with a specific model electrode, where $H = 80$ Å. cDFT predictions for the desalination loop in the presence, and absence, of electrode-grafted polymers, are shown in Fig. 1. We see that the area in the reference case is more than twice as large as with grafted electrodes, and we also need to apply a stronger potential to reach our target.

The above description corresponds to a mean-field treatment of electrostatics. This is motivated by simplicity and the fact that all charges are monovalent. We have established additional support by direct comparisons of desalination loops predicted by cDFT and grand canonical metropolis Monte Carlo (GCMC) simulations. Results from the latter approach are reported in Fig. 8 of Appendix A. The scale is identical in both graphs, allowing direct comparison, and we find satisfactory agreement, considering the coarseness of our model and the qualitative nature of our conclusions. For our model, the simulations

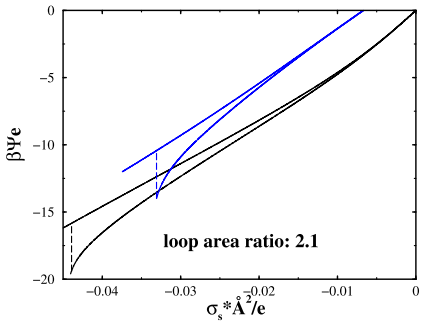


FIG. 1. cDFT predictions of desalination curves, in the presence, and absence, of grafted 8-mer block chains (4 + 4). The surfaces are separated by $H = 80$ Å, and $\xi = 0.65$, which means that the model system is the same as in Fig. 8 of Appendix A. The dashed lines denote the rinsing step, where the concentration in the salt-drained bucket has dropped from 600 mM to $n_s = 1.2 \times 10^{-5}/\text{Å}^3$ (20 mM), chosen as representative of typical potable water. The ratio between the enclosed (loop) areas is about 2.1.

capture all ion correlations, albeit with some statistical noise. There is further support for the mean-field approach. We consider only species carrying at most a single unit of charge, and the high solvent dielectric constant results in weak electrostatic coupling. Härtel *et al.* [16] studied a similar system, and explicit comparisons between cDFT results obtained with ("FMT-PB-MSA") and without ("FMT-PB") an approximation of ion correlations. Their data (cf. Fig. 3 in Ref. [16]) suggest that quantitative differences are small, and of no qualitative significance. Note that the polymers we utilize are overall neutral, so their main response is likely to be dipolar, and thus well described by mean-field methods. Our neglect of explicit water is likely to be a more severe limitation. An explicit representation would approximately capture local and anisotropic variations of the solvent dielectric response, which is not considered with our model. Nevertheless, measuring *difference* quantities likely reduces problems arising from model limitations. We now proceed with mean-field cDFT predictions.

Simple ion density profiles—Let us continue by examining density profiles at high and low applied potentials, comparing data for bare and polymer-covered electrodes. In Fig. 2(a) we see how the polymers effectively generate a double layer even at zero applied potential. Moreover, there is a relative accumulation of cations, with anions being depleted from the slit region. While the cation concentration is vanishingly small near the walls (due to excluded volume and a high concentration of positive monomers), there is a pronounced accumulation of cations outside the dense polymer layer, on account of their affinity to the negative outer part of the polymer brush.

In Fig. 2(b), we display cation density profiles at the "turning point" of the desalination loop (just prior to the rinsing step, denoted by dashed vertical lines in Fig. 1),

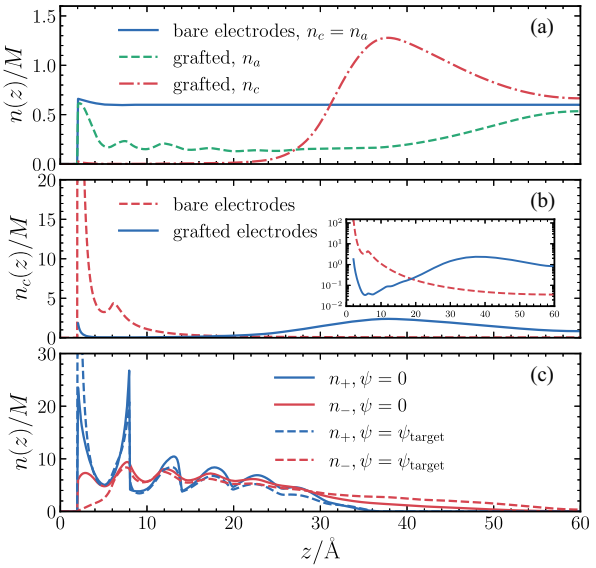


FIG. 2. Ion distribution profiles, at $H = 120$ Å and $\xi = 0.8$, with bare and polymer grafted electrodes. In the latter case, the chains are 12-mers ($6+6-$ block polymers). The applied potential is zero in graph (a), and at the value (Ψ_{target}) for which the bucket salt concentration has dropped to the target value, in graph (b). This means that the absolute value of the Donnan potential is stronger for bare than polymer-grafted electrodes [in graph (b)]. Graph (c) displays monomer density profiles.

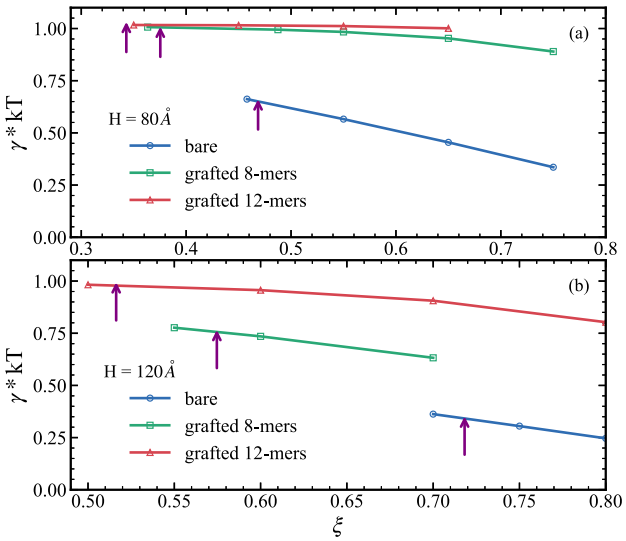


FIG. 3. The dependence of γ on ξ at various separations, for bare and grafted surfaces. The arrows indicate the electrochemically limited maximum performance, γ_{max}, in each case.

i.e., where the bucket salt concentration has dropped to the target value 20 mM, for bare and polymer-covered electrodes (the anions have a very low concentration in both cases). Given that generating density gradients carries a free energy penalty, one might anticipate a lower charging free energy cost with polymer-grafted electrodes than for bare electrodes. This conjecture will be explicitly demonstrated below.

Comparisons of maximum performance—Before we proceed, it is useful to derive a systematic measure of "performance." We can monitor the net uptake of ions within the slit as

$$\langle N_c\rangle_f - \langle N_c\rangle_s + \langle N_a\rangle_f - \langle N_a\rangle_s, \tag{5}$$

where indices "f" and "s" stand for "final" and "start." We can measure $\langle N_c\rangle_f$ as $[\int n_c(final)(z)dz]A$, where A is the area. A reasonable measure of "performance," γ, is how many ions can be extracted from the bucket, for a given energy input; i.e.,

$$\gamma = \frac{(\langle N_c\rangle_f - \langle N_c\rangle_s + \langle N_a\rangle_f - \langle N_a\rangle_s)}{\Delta w}, \tag{6}$$

where Δw is the net work of a cycle, i.e., the area between the two curves in the desalination process.

The performance will depend on the ratio ξ, but also on the separation. Examples are provided in Fig. 3. The arrows mark the points where $\Psi = -|\Psi|_{\text{max}} = -0.615$ V, i.e., the maximum attainable performance at the given separation, as limited by the electrochemical window in aqueous environments (1.23 V between the electrodes). It is clear that the maximum performance benefits from grafted block polymers. There are several reasons for this. We have already mentioned the dramatic drop of density gradients when the polymer layers are in place. Another reason is the dipolar response afforded by the block polymer layer. If we assign a higher dielectric constant to our implicit solvent, we also arrive at increased performance (not shown). Finally, there is a steric aspect. For instance, the nearly identical 8-mer and 12-mer results at $H = 80$ Å can be attributed to a steric saturation effect, discussed below. We have also made tests with a reduced grafting density, resulting in a small drop in desalination performance. An explicit comparison is provided in Appendix C. One observation from Fig. 3 is that the variation of γ with ξ tends to be flatter with polymer-grafted electrodes. This may be useful where a higher ξ, i.e., weaker $|\Psi|_{\text{max}}$, is desirable, perhaps for kinetic reasons, or because one prefers some safety margin for possible onset of redox reactions. Reducing $|\Psi|_{\text{max}}$ can have a dramatic effect, as illustrated in Fig. 4, where we plot the ratio between the maximum performances with and without polymers, at various separations. With a "conservative" limit of 1 V (between the electrodes), our cDFT predicts an improvement in the maximum performance by more than an order of magnitude (!), at a separation of 120 Å.

As stated above, there are also steric mechanisms that promote desalination performance. From Fig. 3 it is obvious that γ_{max} increases as the separation drops, especially for bare electrodes. This is quantified in Fig. 12 of Appendix E, where we note a plateau at very

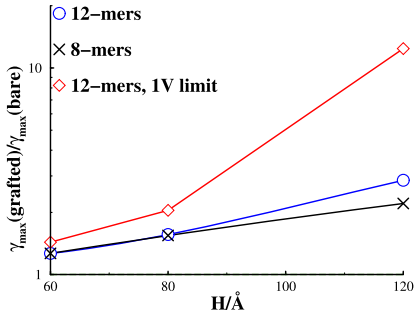


FIG. 4. The ratio between γ_{max}, as obtained with block-polymer grafted and bare electrodes. The solid curves are a guide to the eye.

small separations, with a monotonic decline at larger slit widths. The plateau signifies a confinement saturation effect that is also relevant to polymer-covered electrodes. In Fig. 3, we saw a similar performance at separations of 80 and 120 Å, in the presence of grafted 12-mers. This implies that the saturated "plateau" region is reached already at 120 Å, on account of the thick polymer layers. On the other hand, while grafting by 8-mers gives a similarly high performance at $H = 80$ Å, a further increase to 120 Å leads to a performance drop, commensurate with the "sloping part" of Fig. 12 (Appendix E). Hence, with a thinner layer, confinement saturation manifests itself at shorter separations.

Polymers composed of neutral HS monomers—The relevance of steric exclusion suggests that it might be possible to "mimic" a narrower pore, with increased performance, simply by grafting inert polymers, the monomers of which merely exclude volume. Indeed, the results in Fig. 5 corroborate this conjecture.

The results for 12-mer chains, composed of pure HS monomers are virtually identical to those for 8-mer polyampholytes (compare with Fig. 4). At the largest separation, block-like 12-mers do provide an extra "boost" to the performance. Still, if grafting by simple neutral chains is

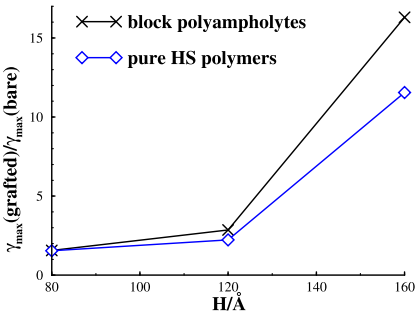


FIG. 5. The ratio between γ_{max}, as obtained with polymer grafted (12-mers) and bare electrodes. Black crosses are results obtained with our "standard" grafted polyampholytes (net neutral), with a block architecture. Blue diamonds are results from calculations with grafted polymers in which *all monomers* are neutral (pure HS monomers).

cheaper or easier to achieve in practice, then this is a viable option, well worth exploring. If one has porous electrodes with a wide pore size distribution, it might be possible to establish a grafting procedure where the polymers (pure HS or block polyampholytes) enter and form grafts within wide pores, but are excluded from narrow pores. This exclusion is, however, not necessarily a problem since the desalination performance is high under those conditions, even with bare electrode surfaces.

Conclusions and outlook—We have shown that polymer grafting provides a simple route to enhance the desalination performance of capacitive deionization (CDI) electrodes without modifying the underlying pore geometry. Both cDFT and GCMC calculations indicate that grafted polymers reduce the charging free energy cost, with steric exclusion providing a substantial contribution and block polyampholytes yielding an additional gain through their dipolar response. Interestingly, even neutral grafts can significantly improve performance, suggesting that interfacial polymer functionalization may be useful for electrodes with relatively wide pores. These results point to polymer grafting as an additional design parameter for membrane-free CDI. Future work should establish how the predicted effects depend on polymer chemistry, grafting density and pore-size distributions, and experiments will be needed to assess the corresponding kinetic and long-term stability aspects. More broadly, similar coupling between polymer conformations, electrostatics, and ion partitioning arises in soft and biological interfaces, suggesting that the mechanisms identified here may help guide studies of ion regulation in such confined environments.

Acknowledgments—J. F. acknowledges financial support by the Swedish Research Council, and computational resources from LUNARC. The cartoon in Fig. 11 was created with the assistance of ChatGPT. We are also grateful for financial support by the Olle Engkvist Foundation (Ref. No: 238-0003).

Data availability—The data that support the findings of this article are available upon request. All codes are publicly available at [35].

[1] UN-Water, Water scarcity, https://www.unwater.org/water-facts/scarcity/ (2024) [accessed: February 17, 2026].
[2] C. J. Vörösmarty, P. B. McIntyre, M. O. Gessner, D. Dudgeon, A. Prusevich, P. Green, S. Glidden, S. E. Bunn, C. A. Sullivan, C. R. Liermann, and P. M. Davies, Nature (London) **467**, 555 (2010).
[3] United Nations World Water Assessment Programme (WWAP), The United Nations world water development report 2023: Partnerships and cooperation for water, Technical Report, UNESCO/UN-Water, 2023 (accessed: February 17, 2026).

[4] M. A. Shannon, P. W. Bohn, M. Elimelech, J. G. Georgiadis, B. J. Mariñas, and A. M. Mayes, Nature (London) **452**, 301 (2008).
[5] U.S. Geological Survey, How much water is there on earth?, https://www.usgs.gov/special-topics/water-science-school/science/how-much-water-there-earth (2023).
[6] M. Prajapati, M. Shah, and B. Soni, Groundwater Sustain. Dev. **19**, 100808 (2022).
[7] L. F. Greenlee, D. F. Lawler, B. D. Freeman, B. Marrot, and P. Moulin, Water Res. **43**, 2317 (2009).
[8] J.-M. Arana Juve, F. M. S. Christensen, Y. Wang, and Z. Wei, Chem. Eng. J. **435**, 134857 (2022).
[9] D. Ben Rouane, A. Ait Errouhi, and R. Mghaiouini, Desalin. Water Treat. **324**, 101578 (2025).
[10] J. Orfi, R. Sherif, and M. AlFaleh, Water **17**, 279 (2025).
[11] V. G. Gude, Water Res. **89**, 87 (2016).
[12] A. K. Khalil, Y. H. Teow, M. Yoshizawa-Fujita, M. Sobri Takriff, A. L. Ahmad, M. A. Atieh, and K. A. Khalil, J. Environ. Chem. Eng. **13**, 118859 (2025).
[13] G. Murphy and D. Caudle, Electrochim. Acta **12**, 1655 (1967).
[14] L. Zou, L. Li, H. Song, and G. Morris, Water Res. **42**, 2340 (2008).
[15] N. Boon and R. van Roij, Mol. Phys. **109**, 1229 (2011).
[16] A. Härtel, M. Janssen, S. Samin, and R. v. Roij, J. Phys. Condens. Matter **27**, 194129 (2015).
[17] M. E. Suss, S. Porada, X. Sun, P. M. Biesheuvel, J. Yoon, and V. Presser, Energy Environ. Sci. **8**, 2296 (2015).
[18] S. Porada, R. Zhao, A. van der Wal, V. Presser, and P. Biesheuvel, Prog. Mater. Sci. **58**, 1388 (2013).
[19] R. Das, M. E. Ali, S. B. A. Hamid, S. Ramakrishna, and Z. Z. Chowdhury, Desalination **336**, 97 (2014).
[20] S. Homaeigohar and M. Elbahri, NPG Asia Mater. **9**, e427 (2017).
[21] M. S. Khan, Z. Y. Leong, D.-S. Li, J. Qiu, X. Xu, and H. Y. Yang, Nanoscale **15**, 15929 (2023).
[22] F. Cheng, Y. Wang, C. Cai, and Y. Fu, Nano Lett. **24**, 9477 (2024).
[23] J.-B. Lee, K.-K. Park, H.-M. Eum, and C.-W. Lee, Desalination **196**, 125 (2006).
[24] F. Yang, Y. He, L. Rosentsvit, M. E. Suss, X. Zhang, T. Gao, and P. Liang, Water Res. **200**, 117222 (2021).
[25] J.-Y. Lee, S.-J. Seo, S.-H. Yun, and S.-H. Moon, Water Res. **45**, 5375 (2011).
[26] M. Ahmad, M. Ahmed, A. Ali, T. A. Wani, K. Khalid, and I. Ali, Desalination **587**, 117925 (2024).
[27] J. A. Regenspurg, W. A. Jonkers, M. A. Junker, I. Achterhuis, E. te Brinke, and W. M. de Vos, Desalination **583**, 117693 (2024).
[28] T. Liu, J. Serrano, J. Elliott, X. Yang, W. Cathcart, Z. Wang, Z. He, and Guoliang Liu, Sci. Adv. **6**, eaaz0906 (2020).
[29] D. Kang, C. Huang, M. Ding, and H. Y. Yang, Desalination **586**, 117884 (2024).
[30] G. Tan, S. Lu, N. Xu, D. Gao, and X. Zhu, Environ. Sci. Technol. **54**, 5843 (2020).
[31] C. E. Woodward, J. Chem. Phys. **94**, 3183 (1991).
[32] S. Haddadi, M. Skepo, and J. Forsman, ACS Nanosci. Au **1**, 69 (2021).
[33] J. Forsman and C. E. Woodward, J. Chem. Phys. **120**, 506 (2004).
[34] F. Xie, C. E. Woodward, and J. Forsman, J. Phys. Chem. B **120**, 3969 (2016).
[35] J. Forsman, Desalination, GitHub repository (2026), https://github.com/janneforsman/desalination.
[36] S. Stenberg, B. Stenqvist, C. Woodward, and J. Forsman, Phys. Chem. Chem. Phys. **22**, 13659 (2020).

End Matter

Appendix A: Simulations—Here, we first need to numerically establish how the salt chemical potential varies with salt concentration in a bulk solution. Since we use Ewald GCMC methods, it is convenient to tabulate how the bulk salt concentration, n_s, varies with the single ion (input) chemical potential (μ_c or μ_a, where $\mu_c = \mu_a$). The results are summarized in Fig. 6.

Given that the dependence shown in Fig. 6 was established, we proceeded with electrode pore simulations, with the pore walls (as in cDFT) being described as flat and infinitely large walls. Specifically, we adopted a newly developed method using single-ion insertions and deletions, combined with an applied electrode (Donnan) potential that regulates the ion accumulation, and therefore the surface charge density. The conducting walls are treated using a 3D Ewald formulation of the Coulomb interactions to deal with the infinite number of image interactions that occur due to multiple reflections across the electrode surfaces [36]. For the symmetric electrolyte model that we consider in this Letter, the individual cation and anion chemical potentials are equal in the bulk solution ($\mu_a = \mu_c$). At each step of the desalination process, we then need to reach consistency between the bucket salt concentration, n_s, as established by Eq. (4), and the chosen ion chemical potential.

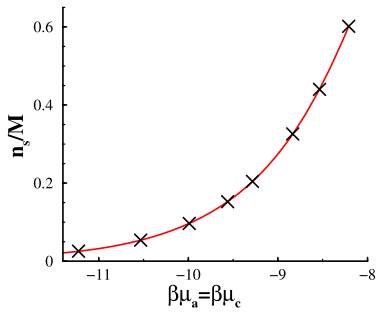


FIG. 6. The dependence of the bucket salt concentration, n_s, on the single ion chemical potential, μ_c [or (μ_a)]. Symbols indicate simulated data points, and the red line marks a cubic spline.

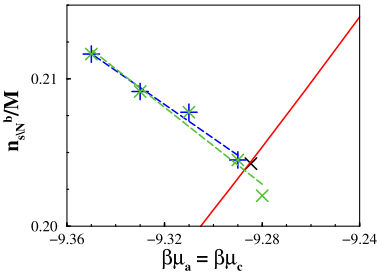


FIG. 7. Simulated search for the correct chemical potential during desalination. In the displayed case (with grafted 8-mers), the Donnan potential is $\beta\Psi e = 8.0$. Blue plus signs denote simulated values of n_s, using average slit densities, and Eq. (4). The black cross symbol indicate an extrapolated target chemical potential. Using these data points (linear regression fit indicated by dashed blue line). The green crosses constitute the same set of data, but with one added measurement, on the other side of the "master curve". The crossing between the corresponding linear regression curve (dashed green) marks an interpolated value, and the difference with the black cross serves as a crude measure of the precision achieved by this approach.

In Fig. 7, we illustrate an iterative search for the appropriate chemical potential, and thus step (ii). We proceed in this manner, with a range of Donnan potentials, until we reach our target, i.e., a Donnan potential strong enough to generate $n_s = 1.2 \times 10^{-5}/\text{Å}^3$, i.e., a bucket salt concentration of about 20 mM. By doing this in the presence, and absence, of grafted 8-mers, we can estimate predicted effects from grafting. An example is shown in Fig. 8.

We are quite happy with the overall agreement with the corresponding cDFT predictions, presented in Fig. 1, even though it is far from perfect.

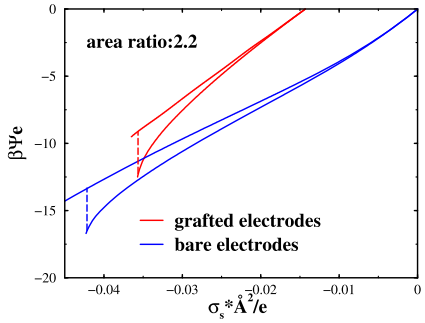


FIG. 8. Simulated desalination curves, in the presence, and absence, of grafted 8-mer block chains. The surfaces are separated by $H = 80$ Å, and $\xi = 0.65$. The dashed lines denote the rinsing step, where the concentration in the salt-drained bucket has dropped from the initial value of 600 mM to $n_s = 1.2 \times 10^{-5}/\text{Å}^3$ (20 mM), chosen as a representative low-salinity condition relevant to potable water. These results can be directly and quantitatively compared with those presented in Fig. 1, where cDFT predictions for the same system are displayed (on the same scale). The ratio between the enclosed (loop) areas is about 2.2.

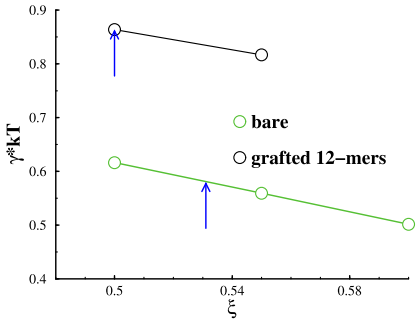


FIG. 9. The dependence of γ on ξ at $H = 120$ Å, for systems in which the particles (monomers and simple ions) are pointlike; i.e., there is no hard-core excluded volume (save the walls).

Appendix B: Systems with vanishing excluded volume—Here we make a brief digression to demonstrate that grafting by net neutral polyampholytes with a block charge structure can improve desalination performance also in the complete absence of monomer and ion hard cores; i.e. there is no excluded volume, except by the walls.

In Fig. 9 we see that, at a separation of 120 Å, $\gamma_{\max}$ increases by about 50% when the electrodes are grafted. This clearly shows that while excluded volume effects are important to the overall CDI performance, the polar response offered by block chains leads to an additional improvement.

Appendix C: The impact of grafting density—In Fig. 10, we compare results obtained with our standard grafting density, $\kappa = 0.02/\text{Å}^2$, with those obtained when this density is reduced by a factor 2. The area increases when the grafting density drops, but the effect is rather small for such a modest change. At very low grafting densities we will of course observe a more significant drop of the efficiency, as the bare electrode result will be approached.

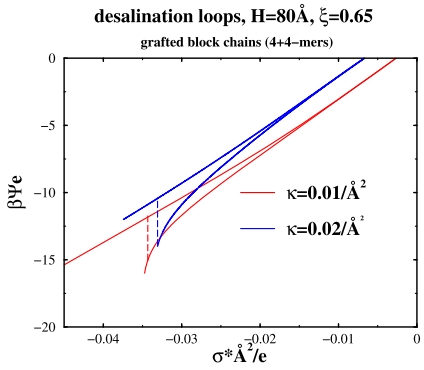


FIG. 10. Desalitation loops at $H = 80$ Å, in the presence of grafted 8-mers, at two different grafting densities.

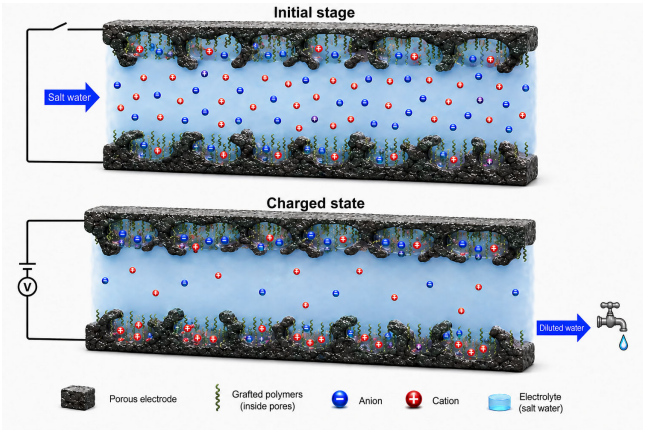


FIG. 11. A cartoon, illustrating two stages of the desalination process. In order to illustrate the pores on the same scale as the electrodes, the pores are shown considerably larger than they actually are. The "real" pores furthermore have a much more elongated shape. Top graph: the initial state, at zero applied voltage, where the region between the two electrodes is filled with salty water. Bottom graph: after completed canonical desalination, the "bucket" volume between the electrodes is desalinated, and fresh water can be extracted.

Appendix D: A schematic illustration—In Fig. 11, we have made a cartoon of the complete desalination system. Since we attempt to illustrate the electrode pores, as well as the overall cell, we are facing the difficulty of mixing microscopic (pores) and macroscopic (electrodes) descriptions. We have thus made the pores much larger and shallower (relatively speaking) than they actually are.

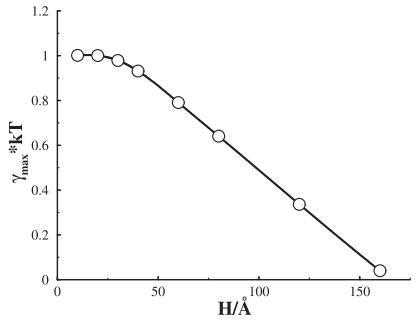


FIG. 12. The variation of $\gamma_{\max}$ with separation, for bare electrodes. The plateau at small H reflects the saturation regime discussed in the text.

Appendix E: Confinement saturation—Figure 12 shows $\gamma_{\max}$ for bare electrodes, as a function of the slit width H. The plateau at small H marks a confinement-saturation regime, followed by a monotonic decrease at larger separations. This behavior provides a reference for the grafted-electrode results discussed in the main text.